Hindawi
Journal of Advanced Transportation
Volume 2019, Article ID 6270515, 15 pages
https://doi.org/10.1155/2019/6270515

*Research Article*

# Optimal Utilization of Adhesion Force for Heavy-Haul Electric Locomotive Based on Extremum Seeking with Sliding Mode and Asymmetric Barrier Lyapunov Function

**Kaihui Zhao**,[1] **Peng Li**,[1] **Changfan Zhang**,[1] **Jing He**,[1] **Xiangfei Li**,[1] **and Jianhua Liu**[2]

[1]*College of Electrical and Information Engineering, Hunan University of Technology, Zhuzhou 412007, China*
[2]*College of Traffic Engineering, Hunan University of Technology, Zhuzhou 412007, China*

Correspondence should be addressed to Jing He; hejing@263.net

Received 1 October 2018; Revised 10 December 2018; Accepted 6 January 2019; Published 23 January 2019

Academic Editor: Andrea Monteriù



An optimal utilization of adhesion force based on extremum seeking with sliding mode (SMES) and asymmetric barrier Lyapunov function (ABLF) is proposed for heavy-haul electric locomotives (HHELs), which can eliminate the wheel skidding at optimal adhesion point and achieves maximum traction for HHELs. First, the state equation of wheel-rail adhesion control system is described. The optimal utilization of adhesion force and anti-slip control are analyzed considering the condition changes at the wheel-rail surface. Then, the nonsingular terminal sliding mode observer (NTSMO) is designed to achieve the accurate adhesion coefficient of the wheel-rail. Finally, the SMES method for HHEL is developed to obtain the optimal slip speed and the maximum adhesion coefficient of the uncertain wheel-rail surface. Meanwhile, the ABLF controller is designed to achieve anti-slip control for HHELs in the optimal adhesion state. Comparing with the conventional differential acceleration control (DAC) method, the simulations and experiments verify that the proposed method can achieve optimal adhesion anti-slip control with quick dynamic response, and the HHEL achieves maximum traction.

## 1. Introduction

Heavy-haul electric locomotives (HHELs) are widely used in railway freight due to its high tractive forces. Taking HXD1F as an example, the HXD1F locomotives are twin unit Bo-Bo+Bo-Bo vehicles, that is two locomotives with 4 axles each. The model has a single axle weight of 30 tons. Single locomotive traction power reaches 9600kW [1]. However, the traction power of the HHELs is limited by the adhesion force between the rail and the wheel. Given that wheel–rail adhesion is affected by temperature, humidity, and surface condition, the adhesion force is nonlinear, uncertain, and time varying [2, 3].

To utilize locomotive traction power effectively, it is necessary to study a control strategy for the HHELs to achieve the maximum adhesion force. This paper proposes a new scheme for the HHELs to optimal utilize of adhesion Force, and the locomotive running at the optimal adhesion point.

The main purpose of optimal adhesion control algorithm is to find the maximum adhesion point to utilize the traction force as much as possible. In recent years, many control methods have been proposed to seek the optimal adhesion point of the wheel-rail. A cellular automata model is suggested and realized multi-objective optimization of automatic train operation system in [4]. An artificial neural network is proposed to determine the optimal coasting speed of train operation for the mass rapid transit system in [5]. Peng et al. seek the optimal adhesion point of wheel-rail surface by calculating the differential value of adhesion force based on differential acceleration control (DAC) method [6, 7]. However, the DAC's disadvantage is unable to completely eliminate the skid phenomenon, and the effect of wheel-rail adhesion disturbances will amplify by differential parts. A train trajectory optimization approach is investigated for mass rapid transit systems in [8]. Most of the above works focus on the optimal adhesion utilization for the locomotive.

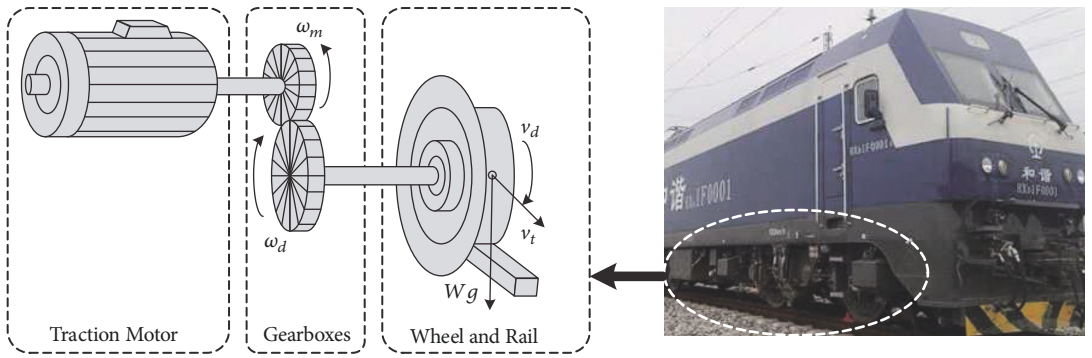


Figure 1: Simplified wheel-rail model of the HHEL.

However, the nonlinearity and parameter disturbances of the wheel-rail is not taken into consideration intensively.

Extreme seeking control (ESC) is a class of control methods, which can autonomously find an optimal system behavior [9]. Extremum seeking with sliding mode (SMES) algorithm was proposed by Davila et al. based on sliding mode control and extreme seeking control theory [10–12]. The algorithm can stabilize a class of systems with optimal parameter uncertain and fast time-varying parameter disturbance, which has applied to many real engineering problems. A new control algorithm of antilock braking system was proposed base on the SMES algorithm to seek the peak point of the tire braking force-slip rate curve [13, 14]. To enhance the dynamic and static performance of the ESC scheme, a novel fast ESC scheme without steady-state oscillation is proposed in [15]. Extreme seeking algorithm is applied to search a maximum or minimum point of the desired behavior or performance for the systems with parametric uncertainties [16]. Furthermore, the anti-slip problem of the wheel–rail at the optimal adhesion state must be considered carefully. The readhesion control strategies were proposed by monitoring the significant fault signal in [17, 18]. The disadvantage of this readhesion control approach is hard to predict the skid phenomenon completely. Recently, the state-constrained control method based on asymmetric barrier Lyapunov function (ABLF) has been paid attention to improve the stability of nonlinear dynamic systems [19]. An aircraft landing control system is designed based on ABLF to achieve unilateral anti-slip constraints and shorten the braking distance of the aircraft [20]. The adaptation of ABLF guarantees that the HHEL operated at a stable region and the optimal adhesion anti-slip control of HHEL is achieved [8]. Inspired by the above work, this paper proposes a new scheme of optimal utilization of adhesion force for the HHEL to achieve the optimal adhesion force based on SMES and ABLF, which can overcome the effects of time-varying parameters of wheel-rail. By constructing an anti-slip controller based on ABLF and SMES, the optimal utilization of adhesion force for the HHEL can be guaranteed effectively.

The remainder of this paper is organized as follows: the wheel-rail mathematical model of the HHEL is described in Section 2. Considering the wheel-rail parameter uncertain, the optimal adhesion point seeking method is proposed based on SMES algorithm in Section 3, and the ultimate convergence is proved. Considering the anti-slip problem at the optimal adhesion point, the anti-slip controller is designed based on ABLF algorithm in Section 4. Compared with the conventional differential acceleration control (DAC) method, simulations and experiments are conducted to verify the effectiveness of the proposed method in Section 5, and Section 6 concludes this paper.

## 2. Wheel-Rail Mathematical Model for the HHEL

The locomotive model is made up of two 4-axis HDX1F locomotives. The locomotive has a single axle weight of 30 ton. The wheel-rail model is composed of three parts, traction motors, gear box, and wheel-rail [8]. The simplified wheel-rail model is shown in Figure 1. The simplified locomotive's traction equipment transmits the traction torque to the wheelsets through the gearboxes and drives the wheel such that it rotates at a speed of $v_d$. During the traction operation process, wheel speed $v_d$ is always greater than vehicle speed $v_t$. The adhesion force $F_\mu$ between the wheel and the rail drives locomotive to move forward [21].

With the damping coefficient ignored, the equation of traction motor is as follows [22]:

$$J_m \frac{d\omega_m}{dt} = T_m - T_L$$
$$T_L \cdot R_g = F_\mu \cdot r \tag{1}$$

where $T_m$ is the electromagnetic torque of the traction motor ($N \cdot m$); $T_L$ is the load torque ($N \cdot m$); $\omega_m$ is the rotor angular velocity ($rad/s$); $\omega_d$ is the angular velocity of the wheel ($rad/s$); $r$ is the radius of the wheel ($m$); $J_m$ is the moment of inertia of the traction motor ($kg \cdot m^2$); $F_\mu$ is the adhesion force between the wheel and the rail ($N$); $R_g$ is the speed ratio of the gear box, $R_g = \omega_m/\omega_d$.

The mechanical dynamics of the HHEL with eight axles is defined as follows [8, 21]:

$$M \frac{dv_t}{dt} = \sum_{i=1}^{8} F_{\mu i} - F_d \tag{2}$$

where $M$ is the total quality of both the locomotive and load ($kg$). $F_{ui}$ is the $i$ axle's adhesion force of the traction

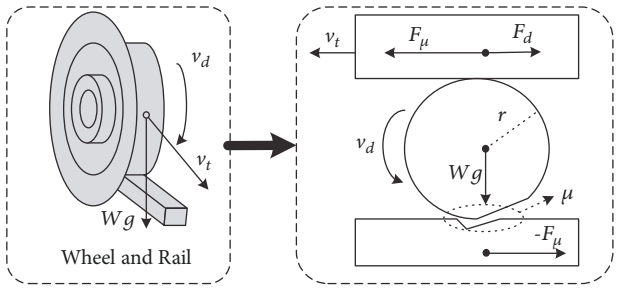


FIGURE 2: Schematic of the wheel-rail adhesion.

motor ($N$). $F_d$ is the sum of resistance forces in the course of locomotive operation ($N$), $F_d = (l + pv_t + qv_t^2) \cdot Mg$ and $l$, $p$, and $q$ are resistance coefficients, which are positive constants.

The schematic of the wheel-rail adhesion is shown in Figure 2. The adhesion coefficient $\mu$ is used to characterize the complex mechanical relationship between the wheel and the rail. The micro-deformation region occurs in the wheel-rail contact region when the wheels rotate with the axle load $W$ [23]. The adhesion force $F_\mu$ is produced by the interaction between the wheel and the rail.

The adhesion force $F_\mu$ and the adhesion coefficient $\mu$ have the following relation:

$$\begin{aligned} F_\mu &= \mu \cdot Wg \\ T_L &= F_\mu \cdot r. \end{aligned} \tag{3}$$

The adhesion coefficient $\mu$ is not only related to the wheel-rail surface but also constrained by creep velocity $v_s$ $(m/s)$. The following empirical equations are derived based on numerous experimental [2]:

$$\begin{aligned} v_s &= v_d - v_t \\ \mu &= ce^{-av_s} - de^{-bv_s} \end{aligned} \tag{4}$$

where $a$, $b$, $c$, and $d$ are the contact's constants, which are positive constants.

State variable is chosen as follows:

$$\begin{aligned} \boldsymbol{x} &= \left[\omega_m \;\; v_s\right]^T, \\ \boldsymbol{u} &= T_m, \\ \boldsymbol{A} &= \left[A_1 \;\; A_2\right]^T, \\ \boldsymbol{F} &= \left[f_1 \;\; f_2\right]^T. \end{aligned} \tag{5}$$

The dynamic model of the HHEL is as follows according to (1):

$$\dot{\boldsymbol{x}} = \boldsymbol{A}\boldsymbol{u} + \boldsymbol{F} \tag{6}$$

where $\boldsymbol{A} = [1/J_m \;\; r/J_m R_g]^T$, $f_1 = -T_L/J_m$, and $f_2 = \overline{f}_2 + \Delta f$. $\overline{f}_2$ is the measurable parameters of HHELs and $\overline{f}_2 = -rT_L/J_m R_g^2 - \dot{v}_t$, $\Delta f$ is an unknown load disturbance. But $\Delta f$ is a bounded quantity, and $|\Delta f| \le \Delta F$.

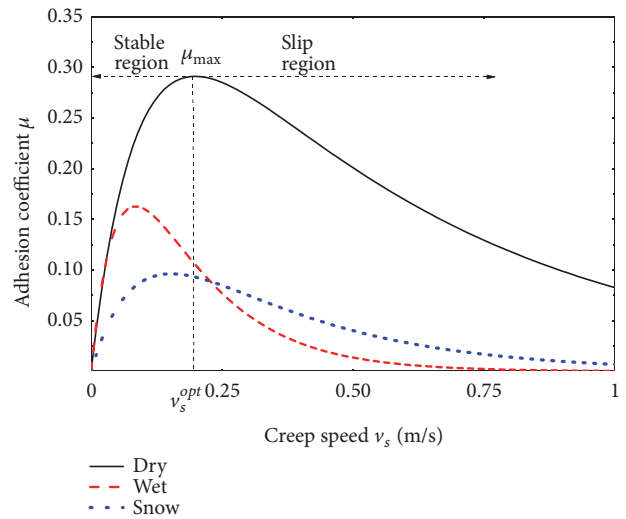


FIGURE 3: Adhesion characteristic curve.

The adhesion characteristic curves under three different wheel-rail surface conditions are shown in Figure 3 [24, 25]. The conclusion can be drawn as follows:

(i) The maximum adhesion coefficients $\mu_{max}$ exist in different wheel-rail surface, which exhibit the same trends.

(ii) The adhesion coefficient increases to $\mu_{max}$ with the increase of $v_s$ in the stable region and then decreases sharply to zero with the increase of creep $v_s$ after crossing the optimal creep velocity $v_s^{opt}$.

(iii) In order to improve the utilization of adhesion force and utilize the locomotive traction motor power effectively, it is necessary to accurately obtain optimal adhesion point of the wheel-rail surface, namely, the maximum adhesion coefficient $\mu_{\max}$ and the optimal creep velocity $v_s^{opt}$.

## 3. Optimal Adhesion Point Seeking Based SMES

Figure 4 shows the schematic of the optimal adhesion SMES method for uncertain wheel-rail surface.

During the traction operation of the HHEL, the nonsingular terminal sliding mode adhesion coefficient observer (NTSMO) is designed to obtain the real-time observation value $\hat{\mu}$ of the wheel-rail adhesion coefficient $\mu$, using the torque $T_m$ and the rotor speed $\omega_m$ of the traction motor. According to the adhesion coefficient observation value $\hat{\mu}$, the unit of extremum seeking with sliding mode iterates the wheel-rail maximum adhesion coefficient $\mu_{\max}$ and obtains the optimal slip speed $v_s^*$.

The unit of anti-slip controller uses the slip speed signal $v_s^*$ to give the torque command $T_m^*$ to control the locomotive, which can make optimal utilization of adhesion force, and the traction motor outputs the maximum traction force.

*3.1. Nonsingular Terminal Sliding Mode Adhesion Coefficient Observer.* Obtaining the real-time adhesion coefficient of the

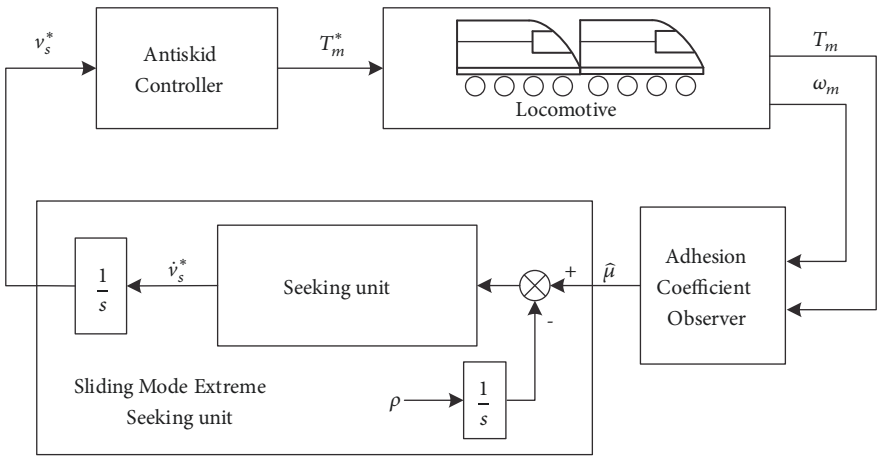


Figure 4: Schematic of extreme-seeking control.

wheel-rail surface is a prerequisite for the extremum seeking with sliding mode method [26]. However, the adhesion coefficient is difficult to measure with general tools. Common processing methods include full-scale state observers, Kalman Filters [27–29].

This paper proposes a nonsingular terminal sliding mode observer (NTSMO) to observe the load torque of the traction motor, and obtain the real-time adhesion coefficient of the wheel-rail [22]. According to (6), the state variables $x_1$ is selected as

$$\begin{aligned} x_1 &= \omega_m \\ \dot{x}_1 &= \frac{1}{J_m} T_m + \frac{1}{J_m} T_L. \end{aligned} \tag{7}$$

The observer is structured as follows:

$$\begin{aligned} \hat{x}_1 &= \hat{\omega}_m \\ \dot{\hat{x}}_1 &= \frac{1}{J_m} T_m + \frac{1}{J_m} v \end{aligned} \tag{8}$$

where the variable $\hat{x}_1$ represents the observed value of $x_1$ and $v$ is the control input vector of observer.

The state estimation error is defined as follows:

$$e_1 = x_1 - \hat{x}_1. \tag{9}$$

Differentiating (9) with respect to time, one obtains

$$\dot{e}_1 = \dot{x}_1 - \dot{\hat{x}}_1 = -\frac{1}{J_m} \left( T_L + v \right). \tag{10}$$

In order to improve the observation accuracy, and reduce the chattering phenomenon of the traditional sliding mode observer, the nonsingular terminal sliding mode observer (NTSMO) is used to observe adhesion coefficient. This paper proposes the following nonsingular terminal sliding mode surface combining the traditional sliding mode surface with the nonsingular terminal sliding mode surface [30]:

$$s_1 = e_1 + \eta_1 \dot{e}_1 + \eta_2 \dot{e}_1^{p/q} \tag{11}$$

where $\eta_1$, $\eta_2$, $p$, and $q$ are the parameters to be designed, which are positive constants, and $p$, $q$ are odd number, $1 < p/q < 2$.

**Theorem 1.** *For the system (7) and the observer (8), if the nonsingular terminal sliding mode surface (11) is selected and the control law (12) is designed, the observation error will convergence to zero in finite time, for any initial value $x_1(0)$ is satisfied $\eta_3 > |\dot{T}_L|$.*

$$\begin{aligned} v = \int_0^t \Bigg[ & \frac{J_m}{\eta_1 + \eta_2 \left( p/q \right) \dot{e}^{p/q-1}} \dot{e}_1 + \left( \eta_3 + \eta_4 \right) \operatorname{sgn}\left( s_1 \right) \\ & + \eta_5 s_1 \Bigg] d\tau. \end{aligned} \tag{12}$$

*Proof.* The Lyapunov function is selected to be

$$V_1 = \frac{1}{2} s_1^2. \tag{13}$$

Differentiating (13) with respect to time, one obtains

$$\begin{aligned} \dot{V}_1 = s_1 \dot{s}_1 &= s_1 \left( \dot{e} + \eta_1 \ddot{e}_1 + \eta_2 \frac{p}{q} \dot{e}_1^{p/q-1} \ddot{e}_1 \right) \\ &= s_1 \left( \eta_1 + \eta_2 \frac{p}{q} \dot{e}_1^{p/q-1} \right) \left( \frac{\dot{e}_1}{\eta_1 + \eta_2 \left( p/q \right) \dot{e}_1^{p/q-1}} + \ddot{e}_1 \right) \\ &= s_1 G \left( \frac{\dot{e}_1}{G} + \ddot{e}_1 \right) \end{aligned} \tag{14}$$

where $G = \eta_1 + \eta_2 p/q \dot{e}_1^{p/q-1}$ and $G > 0$.

Substituting (10) into (15), yields

$$\begin{aligned} \dot{V}_1 &= s_1 G \left( \frac{\dot{e}_1}{G} - \frac{1}{J_m} \left( \dot{T}_L + \dot{v} \right) \right) \\ &= \frac{s_1 G}{J_m} \left( \frac{J_m \dot{e}_1}{G} - \dot{T}_L - \dot{v} \right) \end{aligned}$$

$$= \frac{s_1 G}{J_m}\left(-\dot{T}_L - (\eta_3 + \eta_4)\,\mathrm{sgn}(s_1) - \eta_5 s_1\right)$$
$$= \frac{G}{J_m}\left(-\dot{T}_L s_1 - \eta_3 |s_1| - \eta_4 |s_1| - \eta_5 |s_1|^2\right)$$
$$\leq \frac{G}{J_m}\left(\left(\left|\dot{T}_L\right| - \eta_3\right)|s_1| - \eta_4 |s_1| - \eta_5 |s_1|^2\right). \tag{15}$$

Where $\eta_3$ satisfies $\eta_3 > |\dot{T}_L|$, the following can be obtained:

$$\dot{V}_1 \leq \frac{G}{J_m}\left(-\eta_4 |s_1| - \eta_5 |s_1|^2\right). \tag{16}$$

According to the Lyapunov stability criterion and the sliding mode reachability condition, the error gradually converges to zero in a finite time.

This completes the proof. □

*Remark 2.* Once the system reaches the sliding surface, it is available according to the sliding mode equivalence principle:

$$s_1 = \dot{s}_1 = 0$$
$$e_1 = \dot{e}_1 = 0. \tag{17}$$

Substituting (18) into (10), (19) then will yield

$$\widehat{T}_L = -J_m \eta_1 \,\mathrm{sgn}\, e_1. \tag{18}$$

According to (1) and (19), the observed adhesion coefficient can be obtained as follows:

$$\widehat{\mu} = \frac{R_g}{rWg}\widehat{T}_L. \tag{19}$$

*3.2. Seeking Maximum Adhesion Point by SMES.* The extremum seeking with sliding mode (SMES) [16] can search the maximum adhesion coefficient using the adhesion coefficient observation value. Then, the optimal creep speed is obtained.

The specific design steps are as follows.

*Step 1.* The adhesion coefficient is selected as the input variable and the sliding surface is designed as follows:

$$s_2 = \mu(v_s) - g(t) \tag{20}$$

where $g(t)$ is monotonically increasing at the rate of $\rho$.

The time derivative of (21) is

$$\dot{s}_2 = \frac{d\mu}{dv_s}\dot{v}_s - \rho. \tag{21}$$

*Step 2.* Sliding mode adaptive law is designed as follows:

$$\dot{v}_s = k\,\mathrm{sgn}(\beta) \tag{22}$$

where $k$ and $\alpha$ are positive constants, and $\beta = \sin(\pi s_2/\alpha)$. The symbol function is shown in Figure 5.

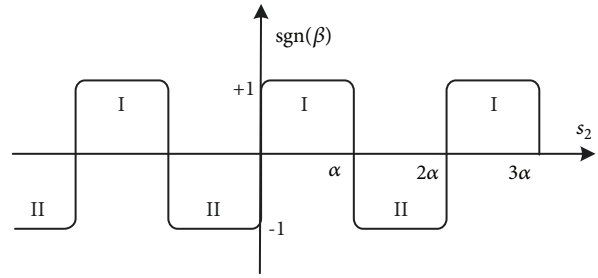


Figure 5: Symbol function.

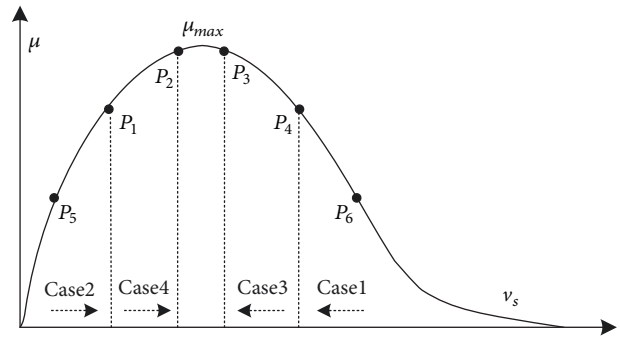


Figure 6: Schematic of SMES.

*Step 3.* Substituting (20) into (12) yields

$$\dot{s}_2 = k\,\mathrm{sgn}(\beta)\frac{\mathrm{d}\mu}{\mathrm{dv_s}} - \rho. \tag{23}$$

*Remark 3.* The schematic of extremum seeking with sliding mode principle (SMES) is shown in Figure 6, and the search process is divided into two phases.

(i) The first phase is to make $v_s$ move from $P_5$ or $P_6$ to $v_s^{opt}$ by SMES. When it arrives at $P_1$ or $P_4$ points, $|d\mu/dv_s|$ gradually becomes smaller. The extreme seeking conditions $d\mu/dv_s > \rho/k$ are no longer satisfied. Then, the searching process enters the second phase.

(ii) When it arrives at $P_3$ and $P_4$, $v_s$ converges to the maximum adhesion point by the vibration integral effect at the second phase.

**Theorem 4.** *Assume that the system (21) meets the following:*

$$\left|\frac{d\mu}{dv_s}\right| > \frac{\rho}{k}. \tag{24}$$

*$s_2$ will gradually converge to the corresponding sliding surface $s_2 = n\alpha$ or $s_2 = (n+1)\alpha$ and $\dot{s}_2 = 0$, where $n$ is a constant determined by the initial $s_2(0)$.*

*Proof.* Assume that the initial value $s_2(0)$ is satisfied as follows:

$$\alpha < s_2(0) < 2\alpha. \tag{25}$$

The adaptive law of (23) has the following form:

$$\mathrm{sgn}(\beta) = -\,\mathrm{sgn}(s_2 - \alpha) = \mathrm{sgn}(s_2 - 2\alpha). \tag{26}$$

The slid region and stable region are analyzed as follows:

*Case 1*. When the creep speed is in the skid region, that is,

$$\frac{d\mu}{dv_s} < -\frac{\rho}{k}. \tag{27}$$

$\dot{s}_2$ can make the following equivalent transformation:

$$\dot{s}_2 = k \operatorname{sgn}(s_2 - 2\alpha)\, dv_s - \rho. \tag{28}$$

Defining variables $\gamma_1 = s_2 - 2\alpha$ yields

$$\begin{aligned} \dot{\gamma}_1 &= \dot{s}_2 \\ \dot{\gamma}_1 &= k \operatorname{sgn}(s_2 - 2\alpha)\, dv_s - \rho. \end{aligned} \tag{29}$$

The convergence of $\gamma_1$ is analyzed as follows:

$$\begin{aligned} \gamma_1 \dot{\gamma}_1 &= -\left|\frac{d\mu}{dv_s}\right| k |\gamma_1| - \rho\gamma_1 \le -\left|\frac{d\mu}{dv_s}\right| k |\gamma_1| + \rho |\gamma_1| \\ &= -|\gamma_1| \left[\left|\frac{d\mu}{dv_s}\right| k - \rho\right] < 0. \end{aligned} \tag{30}$$

Hence, one can easily conclude that $\gamma_1$ will gradually converge to 0 with $\gamma_1 = \dot{\gamma}_1 = 0$, and one can conclude

$$\begin{aligned} \dot{s}_2 &= 0 \\ s_2 &= 2\alpha. \end{aligned} \tag{31}$$

*Case 2*. When the creep speed is in the stable region, that is,

$$\frac{d\mu}{dv_s} > \frac{\rho}{k} \tag{32}$$

According to the same analysis as (29)-(31), one can easily conclude that $\gamma_2 = s_2 - \alpha$ will gradually converge to 0 with $\gamma_2 = \dot{\gamma}_2 = 0$, and one can conclude

$$\begin{aligned} \dot{s}_2 &= 0 \\ s_2 &= \alpha \end{aligned} \tag{33}$$

This completes the proof. □

*Remark 5*. When $\dot{s}_2 = 0$, according to formula (25), the following are obtained:

$$\begin{aligned} \frac{d\mu}{dv_s}\dot{v}_s - \rho &= 0 \\ (\dot{v}_s)_{eq} &= \frac{\rho}{d\mu/dv_s}. \end{aligned} \tag{34}$$

The following conclusions are available:

(i) If $v_s(0) < v_s^{opt}$ and $d\mu/dv_s > \rho/k$, $(\dot{v}_s)_{eq} > 0$ is established and then $v_s$ goes to the optimal adhesion point from the right.

(ii) If $v_s(0) > v_s^{opt}$ and $d\mu/dv_s < -\rho/k$, $(\dot{v}_s)_{eq} < 0$ is established and then $v_s$ goes to the optimal adhesion point from the left.

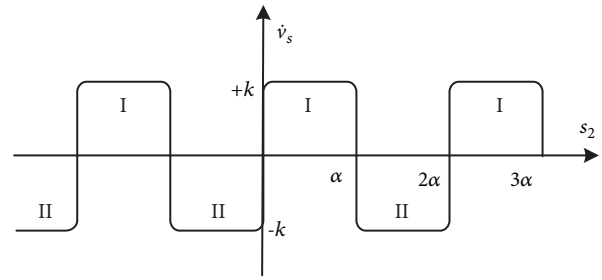


Figure 7: Derivative of the creep speed.

In Figure 6, $P_1$ and $P_4$ represent the critical point of $|d\mu/dv_s| = \rho/k$. Once $v_s \in (P_1, P_4)$, according to (24), the following features exist:

$$\left|\frac{d\mu}{dv_s}\right| \le \left|\frac{\rho}{k}\right| \tag{35}$$

$$\dot{s}_2 = k \operatorname{sgn}(s_2 - 2\alpha) \frac{d\mu}{dv_s} - \rho \le k\frac{d\mu}{dv_s} - \rho < 0. \tag{36}$$

In this case, there is a monotonically decreasing function. There are two deceleration rates:

$$\begin{aligned} (\dot{s}_2)_{\max} &= -\left|\frac{d\mu}{dv_s}\right| k - \rho \\ (\dot{s}_2)_{\min} &= +\left|\frac{d\mu}{dv_s}\right| k - \rho. \end{aligned} \tag{37}$$

The derivative of creep speed is shown in Figure 7. Due to $\dot{s}_2 < 0$, $s_2$ monotonically decreasing. In the process of decrementing, suppose that the total time spent by $s_2$ in Area I is $t_1$ and the total time spent in area II is $t_2$.

In segment $P_1 toP_2$ and $d\mu/dv_s > 0$, the deceleration rate of $s_2$ is faster in area II than area I. This means that the entire search time $t_2 < t_1$, therefore,

$$\int_0^{t_1} \dot{v}_s dt - \int_0^{t_2} \dot{v}_s dt = k(t_1 - t_2) > 0. \tag{38}$$

Therefore, $v_s$ increases in segment $P_1 toP_2$, and it reaches the peak point $v_s^{opt}$.

Similarly, in the segment $P_3 toP_4$, $v_s$ decrements, and it also reaches the peak point.

*Remark 6*. Assuming that the condition of (25) is satisfied and the initial value $s_2(0)$ is at $\alpha < s_2(0) < 2\alpha$, $s_2$ will converge to the corresponding sliding surface of $\alpha$ or $2\alpha$. Once the convergence is completed, $\dot{s}_2 = 0$. Whether $v_s$ is located in the left half or right half of the extreme point $v_s^{opt}$, the creep speed will eventually converge in the neighborhood of the optimal adhesion point $v_s^{opt}$.

Once the extreme seeking is completed, the tracked optimal creep speed is obtained.

$$v_s^* = \int k \operatorname{sgn}\left[\sin\left(\frac{\pi s_2}{\alpha}\right)\right] dt \approx v_s^{opt}. \tag{39}$$

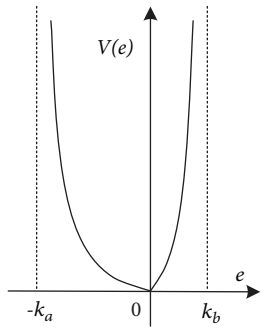


Figure 8: ABLF schematic.

## 4. Design of the Anti-Slip Controller Based on ABLF

The anti-slip control must prevent creep speed from entering the skid region of the adhesion characteristic curves in Figure 3 [2].

According to (6), the state variables $x_2$ are chosen as

$$\dot{x}_2 = A_2 u + f_2 \tag{40}$$

The state estimation error $e_2$ is defined as follows:

$$e_2 = x_2 - v_s^* \tag{41}$$

Differentiating (42) with respect to time, one obtains

$$\dot{e}_2 = A_2 u + f_2 - \dot{v}_s^* \tag{42}$$

Assume that the locomotive is allowed to have an anti-slip range of $D = \{v_s \in R : 0 < v_s < v_s^{opt} + k_b\}$ and $k_b$ is a normal number to be designed. The error is expressed as $D = \{v_s \in R : -v_s^{opt} < e_2 < k_b\}$. The anti-slip control for HHEL is actually the problem of constraint control of the creep speed. In Figure 8, the adhesion curve can be divided into two parts: the stable region $D_a = \{v_s \in R : -k_a < e_2 \le 0\}$ and the skid region $D_b = \{v_s \in R : 0 < e_2 < k_b\}$.

In view of the different anti-slip constraints of the locomotive's stable region and skid region, the following asymmetric barrier Lyapunov function (ABLF) is designed:

$$\begin{aligned} V(e_2) = {} & \frac{1}{2} q(e_2) \log \frac{k_a^2}{k_a^2 - e_2^2} \\ & + \frac{1}{2} (1 - q(e_2)) \log \frac{k_b^2}{k_b^2 - e_2^2}. \end{aligned} \tag{43}$$

The switching function $q(e_2)$ has the following definition:

$$q(e_2) = \begin{cases} 1 & as \ (e_2 \le 0) \\ 0 & as \ (e_2 > 0). \end{cases} \tag{44}$$

Assume that the creep speed is in the allowable anti-slip region $e_2 \in D$. If and only if $e_2 = 0$, $V(e_2) = 0$ if $e_2 \in D$, and if $e_2 \neq 0$, $V(e_2) > 0$ and $V(e_2)$ are continuous. $V(e_2)$ is continuous and positive in the entire anti-slip region.

The following control laws are designed:

$$\begin{aligned} u = {} & \frac{1}{A_2} \left[ \dot{v}_s^* - \left( \overline{f}_2 + \operatorname{sgn}(e_2) F \right) \right] - \frac{1}{A_2} \\ & \cdot e_2 \left[ q(e_2) k_1 \left( k_a^2 - e_2^2 \right) \right. \\ & \left. + (1 - q(e_2)) k_2 \left( k_b^2 - e_2^2 \right) \right] \end{aligned} \tag{45}$$

where $k_1, k_2$ are the positive constants to be designed.

**Theorem 7.** *For the nonlinear system described in (41), if the initial error $e_2(0) \in (-k_a, k_b)$, the error $e_2$ will gradually converge to 0 and will always be constrained in the interval $e_2 \in (-k_a, k_b)$ during the process of convergence.*

*Proof.* The skid region and stable region are analyzed by flowing two cases.

*Case 1.* When the creep speed is in the stable region, that is,

$$\begin{aligned} & q(e_2) = 1 \\ & V(e_2) = \frac{1}{2} \log \left( \frac{k_a^2}{(k_a^2 - e_2^2)} \right) \end{aligned} \tag{46}$$

The time derivative of (47) is

$$\dot{V}(e_2) = \frac{e_2 \dot{e}_2}{k_a^2 - e_2^2} = \frac{e_2}{k_a^2 - e_2^2} \left( A_2 u + f_2 - \dot{v}_s^* \right) \tag{47}$$

The control law $u$ becomes $u_1$:

$$u_1 = \frac{1}{A_2} \left[ \dot{v}_s^* - \left( \overline{f}_2 + \operatorname{sgn}(e_2) F \right) - e_2 k_1 \left( k_a^2 - e_2^2 \right) \right] \tag{48}$$

Substituting (49) into (48) yields

$$\begin{aligned} \dot{V}(e_2) &= \frac{e_2}{k_a^2 - e_2^2} (\Delta f - \operatorname{sgn}(e_2) F) - k_1 e_2^2 \\ &= \frac{1}{k_a^2 - e_2^2} \left( e_2 \Delta f - |e_2| F \right) - k_1 e_2^2 \\ &\le \frac{1}{k_a^2 - e_2^2} \left( |e_2| |\Delta f| - |e_2| F \right) - k_1 e_2^2 \\ &= \frac{|e_2|}{k_a^2 - e_2^2} \left( |\Delta f| - F \right) - k_1 e_2^2 \le -k_1 e_2^2 \end{aligned} \tag{49}$$

It can be seen in the interval $D_a$, $V(e_2) > 0$, and $\dot{V}(e_2) < 0$. If and only if $e_2 = 0$, $\dot{V}(e_2) = 0$.

*Case 2.* When the creep speed is in the skid region, that is,

$$\begin{aligned} & q(e_2) = 0 \\ & V(e_2) = \frac{1}{2} \log \left( \frac{k_b^2}{(k_b^2 - e_2^2)} \right) \end{aligned} \tag{50}$$

The time derivative of (51) is

$$\dot{V}(e_2) = \frac{e_2}{k_b^2 - e_2^2} \left( f_2 + A_2 u - \dot{v}_s^* \right) \tag{51}$$

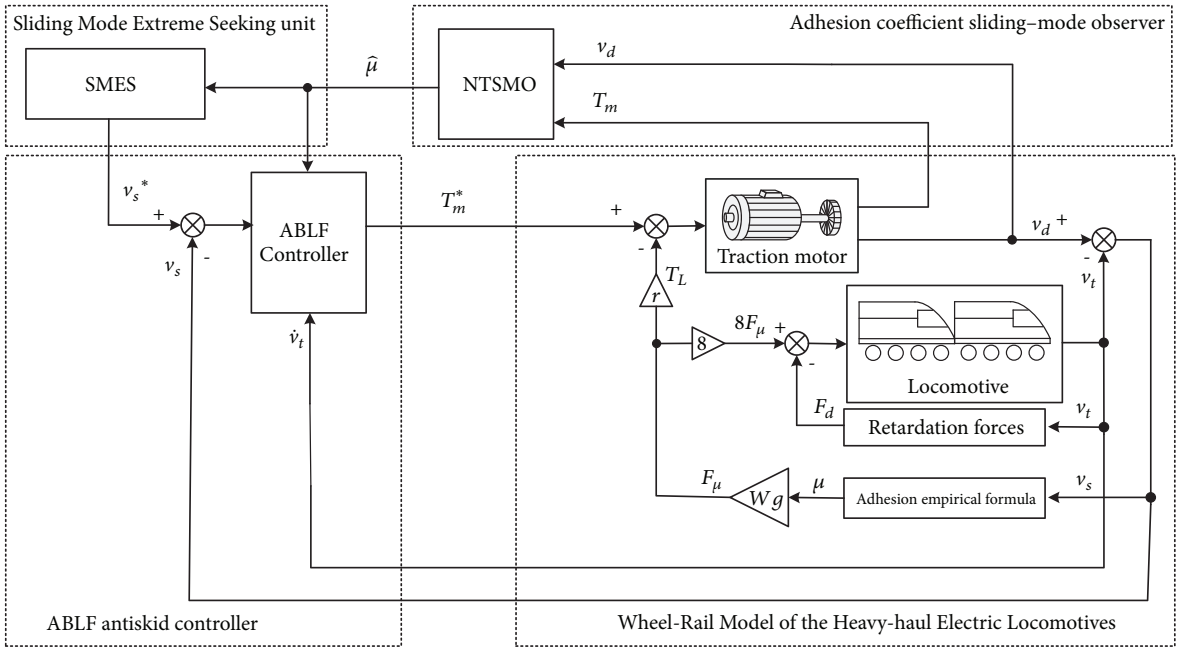


Figure 9: ABLF control block based on Extremum seeking with sliding mode.

The control law $u$ becomes $u_2$

$$u_2 = \frac{1}{A_2}\left[\dot{v}_s^* - \left(\overline{f}_2 + \operatorname{sgn}(e_2)F\right) - e_2 k_2\left(k_b^2 - e_2^2\right)\right] \quad (52)$$

The same analysis process is as (50). Therefore, in the interval $D_b$, $V(e_2) > 0$ and $\dot{V}(e_2) \leq 0$. If and only if $\lim_{e_2 \to 0^+} \dot{V}(e_2) = 0$.

This completes the proof. □

*Remark 8.* In the interval $e_2 \in D, V(e_2)$ is continuous positive definite function and $\dot{V}(e_2)$ is negative and continuous. When the error is close to the anti-slip boundary, $\forall e_2 \longrightarrow -k_a$ or $e_2 \longrightarrow k_b, V(e_2) \longrightarrow \infty$. According to Barbalat Lemma [31], the error $e_2$ will be constrained in anti-slip interval $e_2 \in D$.

According to (42), one obtains

$$-k_a + v_s^*(t) < v_s(t) = e_2(t) + v_s^*(t) < k_b + v_s^*(t) \quad (53)$$

Due to $v_s^*(t) \in (0, v_s^{opt}]$ and $k_a > v_s^{opt}$, $v_s(t) \geq 0$ and then yields

$$0 \leq v_s(t) < k_b + v_s^{opt} \quad (54)$$

By designing $k_b$, it is ensured that the HHEL has good anti-slip performance during tracking the given optimal creep speed $v_s^*$ by SMES.

The proposed optimal adhesion control method for HHEL based on SMES and ABLF is as follows:

(i) The nonsingular terminal sliding mode observer (NTSMO) is designed to observe the adhesion coefficient $\widehat{\mu}$ by (20).

(ii) The observed adhesion coefficient $\widehat{\mu}$ is input to the SMES, the optimal creep speed signal $v_s^*$ is obtained by (40).

(iii) The estimated creep speed $v_s^*$ is input to the ABLF anti-slip controller, and the given torque command $T_m^*$ is calculated according to (46). The optimal utilization of adhesion force for the HHEL can be guaranteed.

## 5. Simulation and Experiment

Figure 9. shows the diagram of the model of optimal utilization of adhesion force for HHEL based on SMES and ABLF. The simulation model is divided into four parts, namely, wheel-rail model of the HHEL, the adhesion coefficient nonsingular terminal sliding mode observer (NTSMO), Extremum seeking with sliding mode (SMES) and ABLF anti-slip controller. Table 1 presents the simulation parameters of HHEL, and Table 2 shows the parameters of adhesion characteristics of three different rail surfaces of dry, wet, and snow [2, 8].

In order to verify the robustness of the proposed method in this paper, the simulated wheel-rail surface changes are simulated. The simulated wheel-rail surface gradually deteriorates, the 0-5s wheel-rail surface is dry, and the 5-10s wheel-rail surface is damp. 10-15s rail surface is rain and snow. The running resistance coefficient is $l = 0.5$, $p = 0.041$, and $q = 0.0022$. The parameters of SMES are designed as $\rho = 1$, $k = 1$, and $\alpha = 0.05$. The gain of ABLF anti-slip controller is designed as follows: $k_1 = k_2 = 1000$, $k_b = 0.01$, and $k_a = v_s^{opt} + k_b$.

*5.1. Simulations.* The simulation waveforms are shown in Figures 10–15. Figure 10 shows the observed values and actual values of the adhesion coefficient observed by the nonsingular terminal sliding mode observer. The observed value tracks

Table 1: Parameters of heavy-haul locomotive.

| Parameters | Description | Values |
|---|---|---|
| $M$ | Total quality of the locomotive and load | 6000 $ton$ |
| $W$ | Single axle load of the locomotive | 30 $ton$ |
| $J_m$ | Inertia moment of motor | 11 $kg.m^2$ |
| $r$ | Wheel radius | 0.625 $m$ |
| $R_g$ | Gear speed transfer ratio | 6.294 |

Table 2: Parameters of Three kinds of surface adhesion.

| Rail surface | Optimal creep speed | Adhesion coefficient maximum |
|---|---|---|
| Dry | 0.2 $m/s$ | 0.29 |
| Wet | 0.085 $m/s$ | 0.16 |
| Snow | 0.153 $m/s$ | 0.09 |

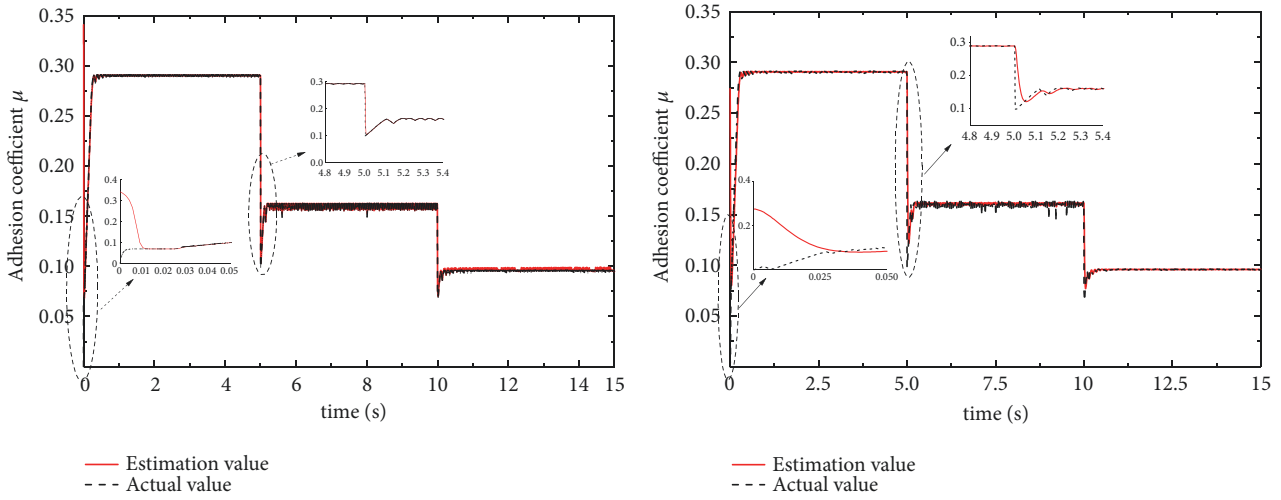


(a) NTSMO (b) FDSO

Figure 10: Actual value and observed value of the adhesion coefficient.

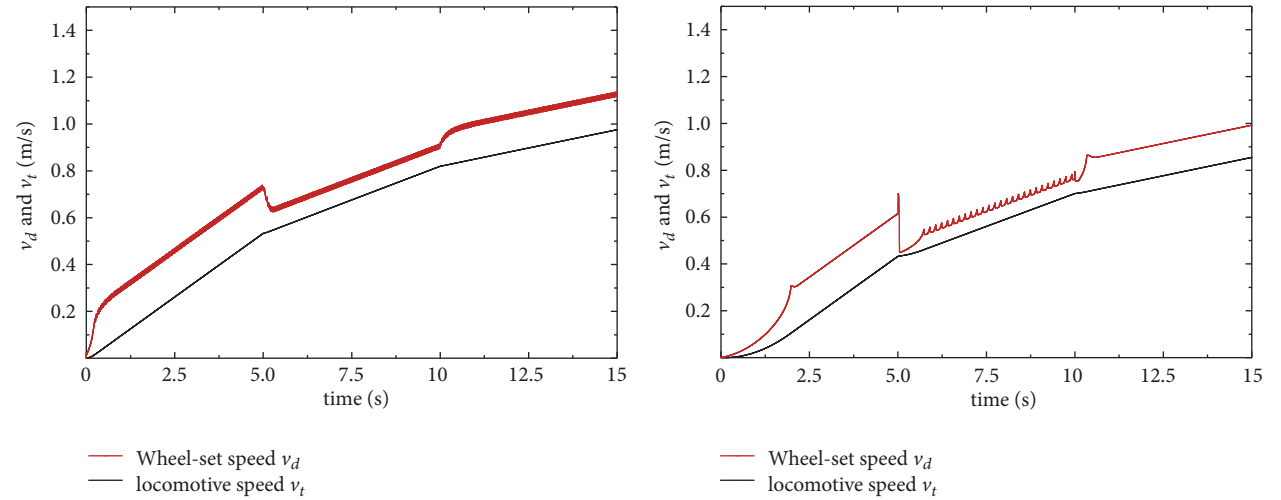


(a) SMES method (b) DAC method

Figure 11: Wheel-set speed and locomotive speed.

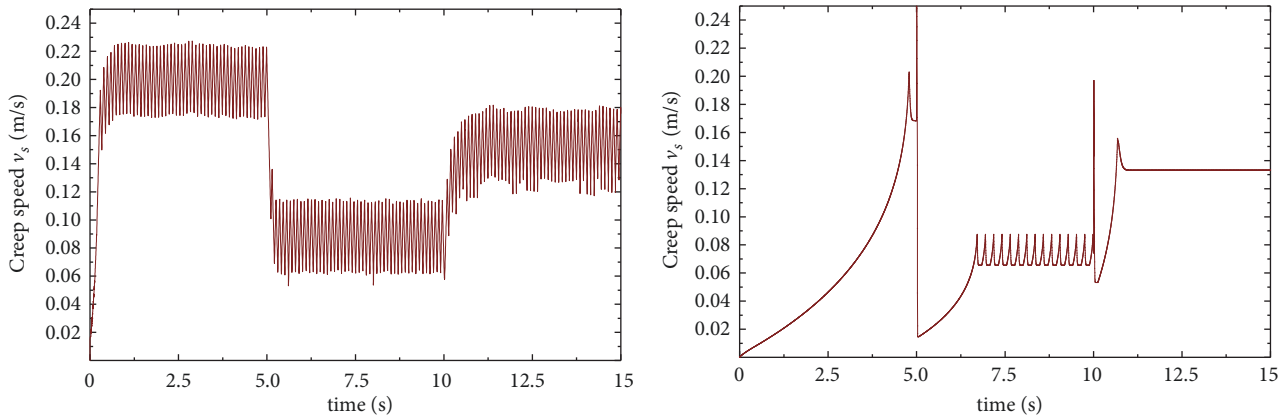


(a) SMES method (b) DAC method

Figure 12: Creep speed.

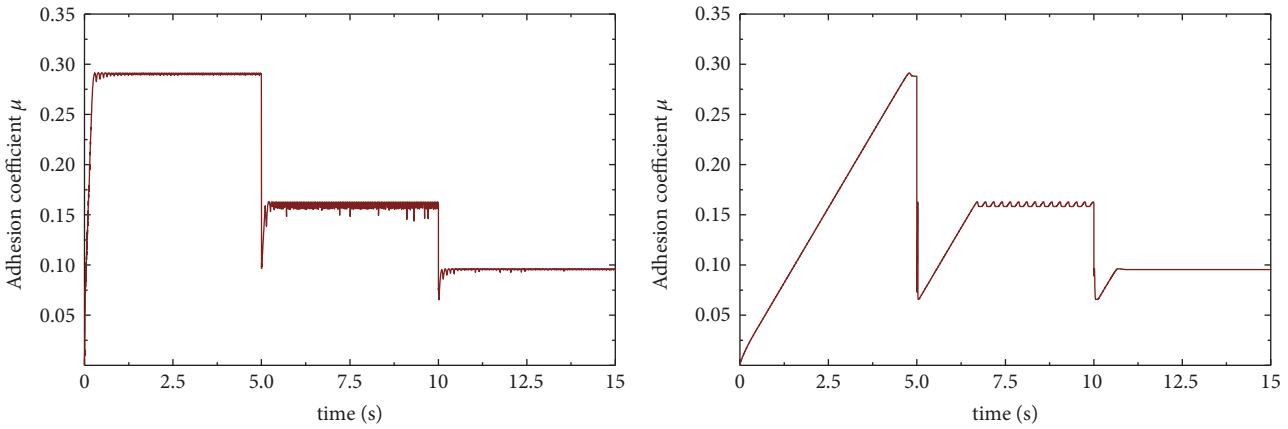


(a) SMES method (b) DAC method

Figure 13: Adhesion coefficients.

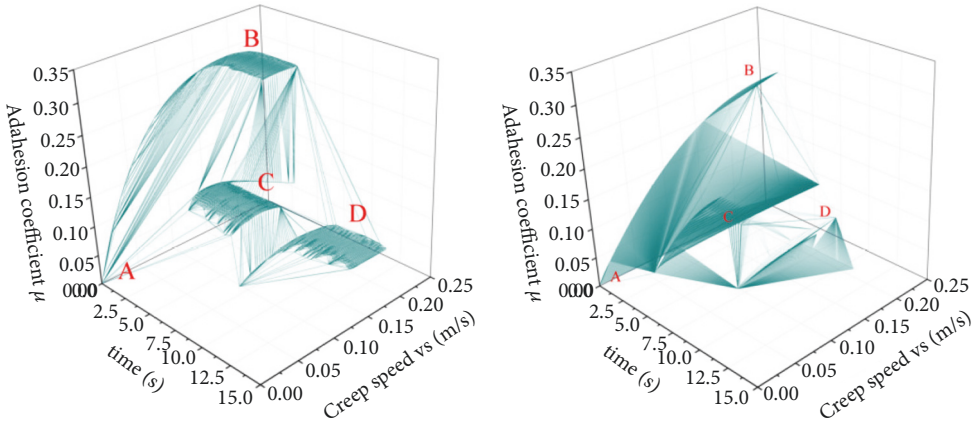


(a) SMES method (b) DAC method

Figure 14: Adhesion characteristic curve.

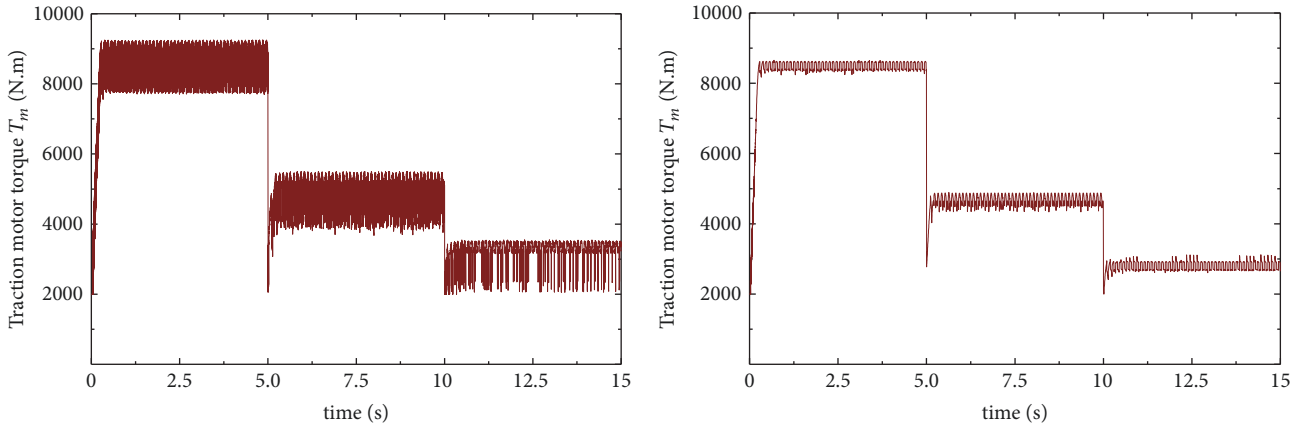


(a) Sliding mode controller

(b) ABLF controller

Figure 15: Traction motor torque.

the actual value of the adhesion coefficient at 0.025s. At the time of 5s and 10s, the observer maintains a good observation accuracy and achieves the desired observation target.

In order to verify the performance of the proposed SMES and ABLF algorithm, the comparing simulation is conducted with the differential acceleration control (DAC) method. Figure 11 shows the wheel-rail speed and locomotive speed of the sliding mode extreme seeking algorithm and the DAC method. Figure 12 shows the creep speed of the sliding mode extreme seeking algorithm and the DAC method. From Figures 11 and 12, it can be seen that the extreme seeking unit accurately searches the best slip speed of the dry track at 0.2 (m/s) in the neighborhood after a search time of 1(s). When the rail surface switches to wet at 5(s), extremum seeking with sliding mode unit according to the adhesion coefficient observed value changes and the slip speed search value stabled in 0.08(m/s) after 0.8(s). When the rail surface is switched to snow rail surface, the sliding mode extreme unit still maintains good search results. In Figure 12(b), differential modules in the DAC method cause a sharp fluctuation in the slip speed and the search speed is slow at the start. Figure 13 shows the waveforms of the adhesion coefficients of the two search algorithms. The sliding mode extreme seeking algorithm has a faster response time.

Figure 14 shows a three-dimensional map of the adhesion characteristic. The locomotive starts from point A on the dry rail surface, the adhesion state moves toward the best adhesion point B, and the adhesion coefficient is finally in $\mu = 0.29$. Then, the rail surface switched into the wet rail surface. The adhesion state moves toward the optimal adhesion point C, and the adhesion coefficient is $\mu = 0.16$. Finally, the rail surface switched into the snow rail surface. The adhesion point moves toward the adhesion point D. Eventually, the adhesion coefficient is in$\mu = 0.09$. In Figure 14(b), the traditional DAC method has a sharper fluctuation due to the creep speed, which results in poor stability of the adhesion characteristic curve.

Figure 15(a) is the output torque waveform of the conventional sliding mode control anti-slip controller. The conventional sliding mode anti-slip control algorithm has larger torque fluctuations in output traction torque. Figure 15(b) is the output torque waveform of the ABLF controller designed in this paper. The output torque waveform of the ABLF anti-slip controller is stable and the amplitude is small, which effectively reduces the loss during locomotive operation and is beneficial to prolong the life cycle of the wheel-rail.

*5.2. Experiments.* The real locomotive operating environment is difficult to rely on simulation soft. This work uses the RT-lab experimental platform to conduct semiphysical experiments. Figure 16 shows the RT-Lab experimental platform used in this work. The C program code of the SMES optimal adhesion utilization and ABLF anti-slip controller is downloaded to the DSP controller TMS320F2812 using a PC. Then, the HHEL model is compiled into OP5600, and the HILS of the optimal adhesion utilization system of the HHEL can be realized. Figure 17 presents the RT-Lab HILS configuration diagram of the SMES optimal adhesion control system of the HHEL. The experimental results are shown in Figures 18–21.

In Figure 18, the experimental results of the conventional FDSO and NTSMO under the condition of wheel-rail parameter uncertain are shown. By contrast, the proposed NTSMO method exhibits a faster response speed then the conventional FDSO. Figure 19 shows the creep speed seeking response comparisons of the conventional DAC method and SMES method under rapid changes of wheel-rail. Adhesion coefficient is based on DAC method and SMES methods as shown in Figure 20. The experimental results indicate that the SMES method can improve the robustness against parameter uncertain. Figure 21 shows the torque response comparisons of the sliding mode controller and ABLF controller. The ABLF control strategy clearly shows good control precision in the steady state and avoids the chattering of the sliding mode control method.

## 6. Conclusions

This paper proposes a novel optimal utilization of adhesion force for HHEL considering wheel-rail parameter uncertain

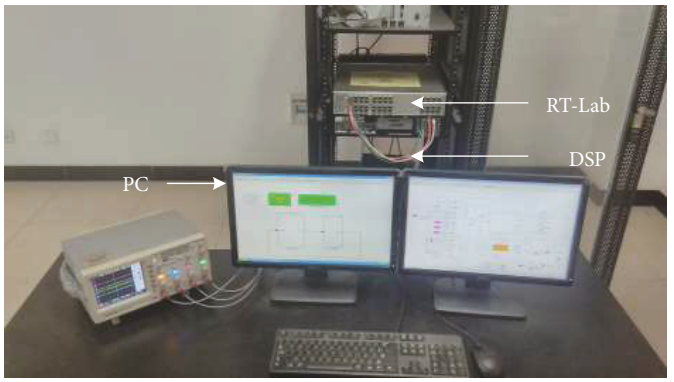


Figure 16: RT-Lab experimental platform.

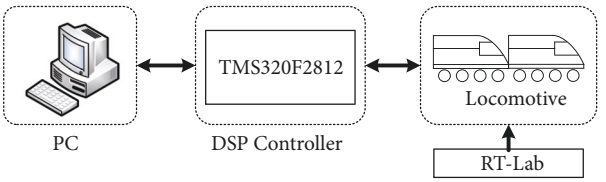


Figure 17: Loop system configuration diagram of RT-Lab.

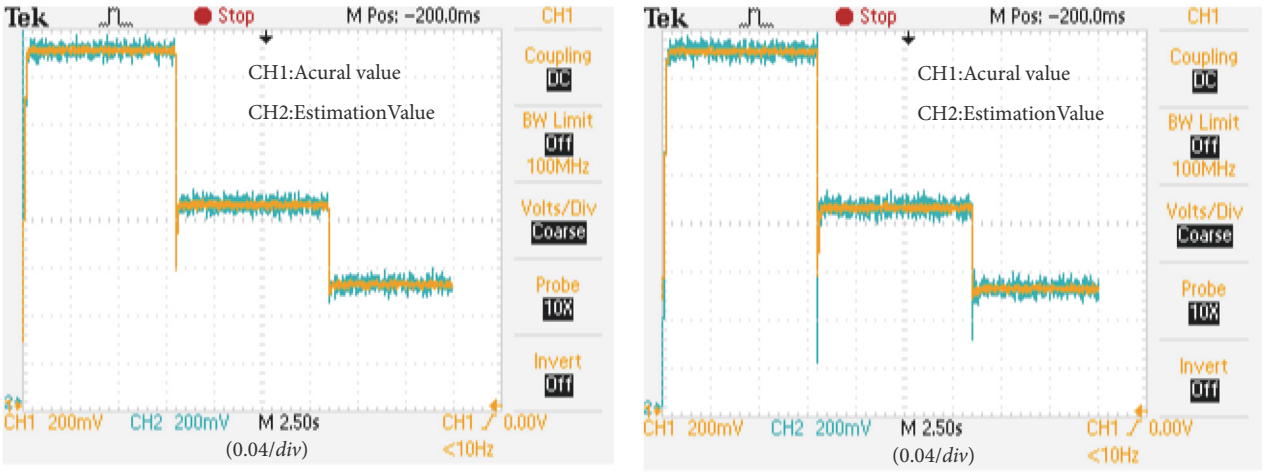


(a) NTSMO

(b) FDSO

Figure 18: Actual value and observed value of the adhesion coefficient.

based on SMES and ABLF. The wheel-rail adhesion coefficient can be achieved precisely by the designed nonsingular terminal sliding mode observer (NTSMO). The optimal adhesion point of the uncertain wheel-rail surface can be searched online based on the designed extremum seeking with sliding mode (SMES) method. The designed ABLF controller can achieve anti-slip control for HHELs in the optimal adhesion state. The proposed method can achieve optimal adhesion anti-slip control, and the HHEL achieves maximum traction. It ensures the safety while realizing the optimal utilization adhesion Force for HHEL.

## Data Availability

The data of the locomotive and adhesion conditions used to support the findings of this study are included within the article. The model data of matlab and RT-lab used to support the findings of this study are available from the corresponding author upon request.

## Conflicts of Interest

The authors declare that they have no conflicts of interest.

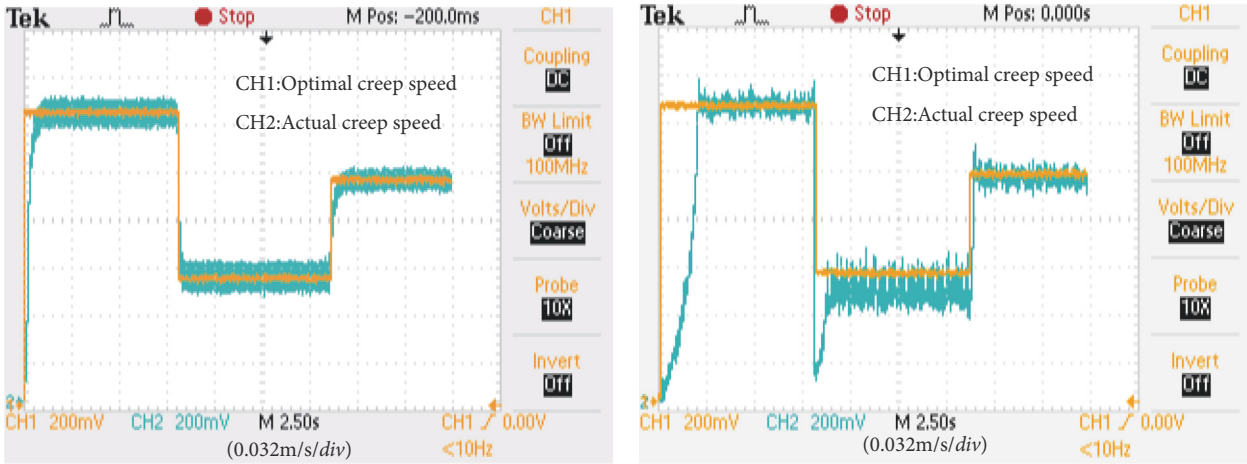


(a) SMES method (b) DAC method

Figure 19: Slip speed.

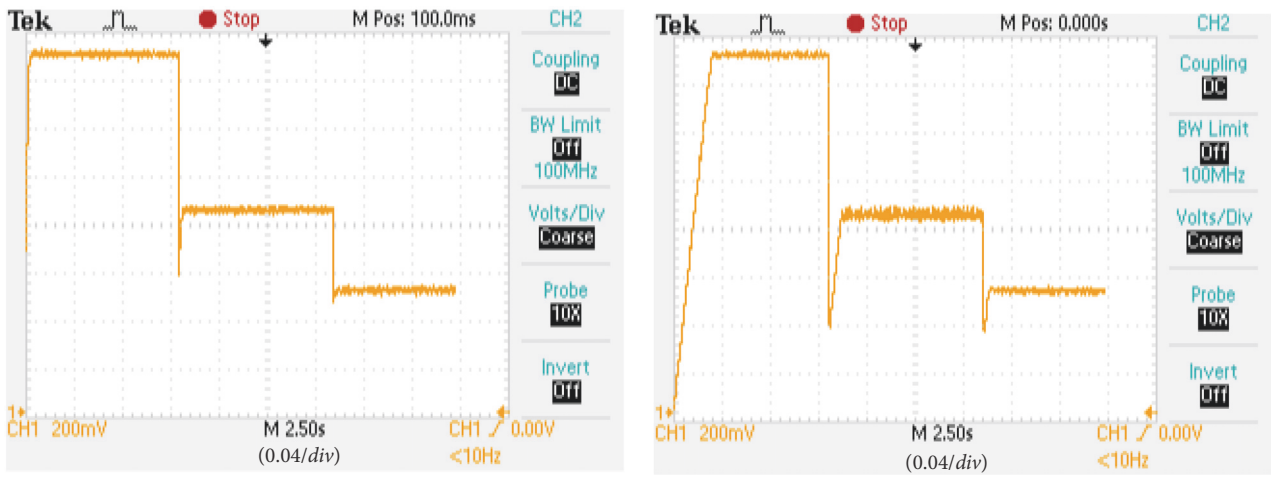


(a) SMES method (b) DAC method

Figure 20: Adhesion coefficients.

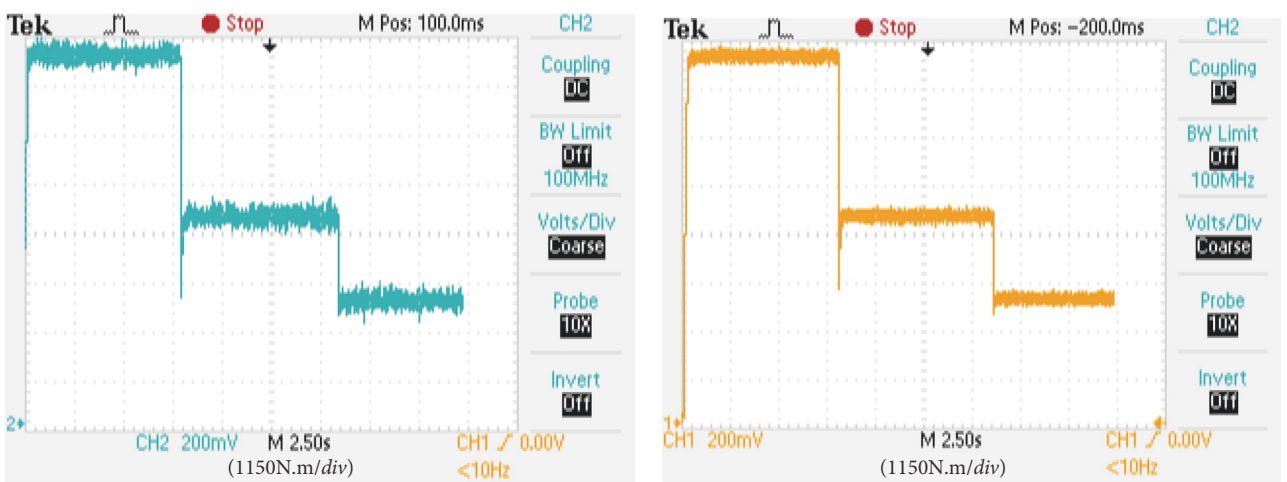


(a) Sliding mode controller (b) ABLF controller

Figure 21: Traction motor torque.

## Acknowledgments

This work was supported in part by the Natural Science Foundation of China under Grant nos. 61773159 and 61503131, in part by the Hunan Provincial Natural Science Foundation of China under Grant nos. 2018JJ2093, 2018JJ4066, 2017JJ4031, and 2016JJ5012, in part by the Scientific Research Fund of the Hunan Provincial Education Department under Grant no. 17B073, and in part by the Key Laboratory for Electric Drive Control and Intelligent Equipment of Hunan Province Grant no. 2016TP1018.

## References

[1] Y. Hu, "Current status and development trend of technology system for railway heavy haul transport in China," *Zhongguo Tiedao Kexue/China Railway Science*, vol. 36, no. 2, pp. 1–10, 2015.

[2] J. Li, Y. Hu, H. Peng, and L. Liu, "Key techniques and design methods of adhesion control in rail transportation," *Electric Drive for Locomotives*, no. 6, pp. 1–5, 2014.

[3] Y. Yao, H.-J. Zhang, Y.-M. Li, and S.-H. Luo, "The dynamic study of locomotives under saturated adhesion," *Vehicle System Dynamics*, vol. 49, no. 8, pp. 1321–1338, 2011.

[4] P. E. Orukpe, X. Zheng, I. M. Jaimoukha, A. C. Zolotas, and R. M. Goodall, "Model predictive control based on mixed H2/H∞ control approach for active vibration control of railway vehicles," *Vehicle System Dynamics*, vol. 46, no. 1, pp. 151–160, 2008.

[5] H.-J. Chuang, C.-Y. Ho, C.-S. Chen, C.-S. Chen, C.-H. Lin, and C.-H. Hsieh, "Design of Optimal Coasting Speed for MRT Systems Using ANN Models," *IEEE Transactions on Industry Applications*, vol. 45, no. 6, pp. 2090–2097, 2009.

[6] H. Peng, H. Chen, Y. Zeng et al., "Simulation of adhesion control method based on differential acceleration," *Electric Drive for Locomotives*, no. 2, pp. 26-27, 2010.

[7] G. Xu, K. Xu, C. Zheng, and T. Zahid, "Optimal operation point detection based on force transmitting behavior for wheel slip prevention of electric vehicles," *IEEE Transactions on Intelligent Transportation Systems*, vol. 17, no. 2, pp. 481–490, 2016.

[8] K. Zhao, P. Li, C. Zhang, J. He, Y. Li, and T. Yin, "Online Accurate Estimation of the Wheel-Rail Adhesion Coefficient and Optimal Adhesion Antiskid Control of Heavy-Haul Electric Locomotives Based on Asymmetric Barrier Lyapunov Function," *Journal of Sensors*, vol. 2018, Article ID 2740679, 12 pages, 2018.

[9] C. Zhang and R. Ordonez, *Extremum-seeking control and applications - A Numerical Optimization-Based Approach*, Springer Science and Business Media, London, UK, 2011.

[10] H. S. Tsien, *Engineering Cybernetics*, McGraw-Hill, New York, NY, USA, 1954.

[11] S. Drakunov and U. Ozgune, "Optimization of nonlinear system output via sliding mode approach," in *Proceedings of the in IEEE International Workshop on Variable Structure and Lyapunov Control of Uncertain Dynamical System*, pp. 61-62, Sheffield, UK, 1992.

[12] B. Zuo, Y. Hu, and J. Shi, "Research and development of extremum seeking algorithm," *Journal of Naval Aeronautical and Astronautical University*, vol. 21, no. 6, pp. 611–617, 2006.

[13] B. Zhou, M. Xu, X. Yuan, and L. Fan, "Acceleration slip regulation based on extremum seeking control with sliding mode," *Journal of Mechanical Science and Technology*, vol. 46, no. 2, pp. 307–311, 2015.

[14] B. Zhou, Y. Li, X. Yuan, X. Hu, and Y. Cheng, "Sliding mode extremum-seeking algorithm for control of abs with vehicle lateral stability improvement," *Journal of Vibration and Shock*, vol. 35, no. 4, pp. 121–126, 2016.

[15] L. Wang, S. Chen, and K. Ma, "On stability and application of extremum seeking control without steady-state oscillation," *Automatica*, vol. 68, pp. 18–26, 2016.

[16] E. Dincmen, "Extremum seeking control of uncertain systems," *TWMS Journal of Applied and Engineering Mathematics*, vol. 7, no. 1, pp. 131–141, 2017.

[17] T. Hara and T. Koseki, "Study on re-adhesion control by monitoring excessive angular momentum in electric railway tractions," in *Proceedings of the 12th IEEE International Workshop on Advanced Motion Control (AMC '12)*, pp. 1–6, IEEE, Sarajevo, Bosnia and Herzegovina, March 2012.

[18] M. Yamashita and T. Soeda, "Anti-slip re-adhesion control method for increasing the tractive force of locomotives through the early detection of wheel slip convergence," in *Proceedings of the 17th European Conference on Power Electronics and Applications, EPE-ECCE Europe '15*, pp. 1–10, Geneva, Switzerland, 2015.

[19] C. Wenchuan, L. Danyong, and L. S. Yongduan, "A novel approach for active adhesion control of high-speed trains under antiskid constraints," *IEEE Transactions on Intelligent Transportation Systems*, vol. 16, no. 6, pp. 3213–3222, 2015.

[20] X. Chen, Z. Dai, H. Lin, Y. Qiu, and X. Liang, "Asymmetric Barrier Lyapunov Function-Based Wheel Slip Control for Antilock Braking System," *International Journal of Aerospace Engineering*, vol. 2015, Article ID 917807, 10 pages, 2015.

[21] Q. Ren, *Design and simulation of heavy haul locomotives and trains, [Master thesis]*, Southwest Jiaotong University, Chengdu, China, 2014.

[22] K. Zhao, T. Chen, C. Zhang, J. He, and G. Huang, "Sensorless and torque control of IPMSM applying NFTSMO," *Yi Qi Yi Biao Xue Bao/Chinese Journal of Scientific Instrument*, vol. 36, no. 2, pp. 294–303, 2015.

[23] M. Spiryagin, P. Wolfs, C. Cole, and V. Spiryagin, *Design and Simulation of Heavy Haul Locomotives and Trains*, CRC Press, Florida, FL, USA, 2016.

[24] O. Polach, "Creep forces in simulations of traction vehicles running on adhesion limit," *Wear*, vol. 258, no. 7-8, pp. 992–1000, 2005.

[25] J. Li, H. Chen, Z. Zhang, J. Hu, and L. Xu, "Deload algorithm for highly effective spressing locomotive slip and slide," *Electric Drive for Locomotives*, vol. 6, pp. 6–10, 2015.

[26] C. Zhang, J. Sun, J. He, and L. Liu, "Online Estimation of the Adhesion Coefficient and Its Derivative Based on the Cascading SMC Observer," *Journal of Sensors*, vol. 2017, Article ID 8419295, 11 pages, 2017.

[27] C. Zhang, Y. Huang, and R. Shao, "Robust sensor faults detection for induction motor using observer," *Control Theory and Technology*, vol. 10, no. 4, pp. 528–532, 2012.

[28] P. Pichlík and J. Zdênek, "Extended Kalman filter utilization for a railway traction vehicle slip control," in *Proceedings of the 2nd International Conference on Optimization of Electrical and Electronic Equipment, OPTIM 2017 and Intl Aegean Conference on Electrical Machines and Power Electronics, ACEMP '17*, pp. 869–874, Brasov, Romania, May 2017.

[29] W. Lin, Z. Liu, and Y. Fang, "Re-adhesion optimization control strategy for metro traction," *Xinan Jiaotong Daxue Xuebao/Journal of Southwest Jiaotong University*, vol. 47, no. 3, pp. 465–470, 2012.

[30] Y.-M. Wang, Y. Feng, H.-W. Xia, and L.-Q. Shen, "Smooth nonsingular terminal sliding mode control of uncertain multiinput systems," *Kongzhi yu Juece/Control and Decision*, vol. 30, no. 1, pp. 161–165, 2015.

[31] J. A. Gallegos, M. A. Duarte-Mermoud, N. Aguila-Camacho, and R. Castro-Linares, "On fractional extensions of Barbalat Lemma," *Systems & Control Letters*, vol. 84, pp. 7–12, 2015.